

**Petrology and tectono-metamorphic
evolution of amphibolite to granulite facies rocks of the
Bundelkhand Craton, Jhansi, India**



*Thesis Submitted in partial fulfilment
for the Award of Degree*

Doctor of Philosophy

By

Pratigya Pathak

**DEPARTMENT OF CIVIL ENGINEERING
INDIAN INSTITUTE OF TECHNOLOGY
(BANARAS HINDU UNIVERSITY)**

VARANASI - 221005

INDIA

Roll No. 17061004

2022

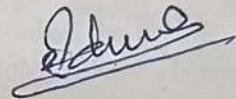
THESIS CERTIFICATE

This is certified that the work contained in this thesis titled "**Petrology and tectono-metamorphic evolution of amphibolites to granulite facies rocks of the Bundelkhand craton Jhansi, India**" submitted by "**Pratigya Pathak**" to the Indian Institute of Technology (BHU), Varanasi has been carried out under my supervision and that this work has not been submitted elsewhere for a degree.

It is further certified that the student has fulfilled all the requirements of Comprehensive Examination, Candidacy and SOTA for the award of Ph.D. Degree.

Varanasi – 221005

Date: 8/9/2022



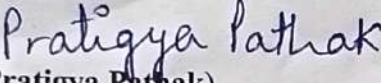
Prof. S. B. Dwivedi

(Supervisor)

Department of Civil Engineering
Indian Institute of Technology (BHU)
Varanasi – 221005, India

DECLARATION BY THE STUDENT

I, "Pratigya Pathak", certify that the work embodied in this thesis is my own bona fide work and carried out by me under the supervision of "Prof. S. B. Dwivedi" from July 26, 2017 to July 26, 2022, at the "Department of Civil Engineering", Indian Institute of Technology (BHU), Varanasi. The matter embodied in this thesis has not been submitted for the award of any other degree/diploma. I declare that I have faithfully acknowledged and given credits to the research workers wherever their works have been cited in my work in this thesis. I further declare that I have not willfully copied any other's work, paragraph, text, data, results, etc., reported in journals, books, magazines, reports dissertations, theses, etc., or available at websites and have not included them in this thesis and have not cited as my own work.

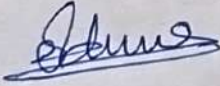

(Pratigya Pathak)

Place: IIT (BHU), Varanasi

Date: 8/9/2022


DECLARATION BY THE SUPERVISOR

It is certify that the above statement made by the student is correct to the best of my knowledge.



(Prof. S. B. Dwivedi)

Supervisor
Supervisor
Department of Civil Engineering
Indian Institute of Technology, (BHU)
Varanasi-221005



Head of Department
विभागाध्यक्ष/HEAD

जानपद अभियांत्रिकी विभाग
Department of Civil Engineering
भारतीय प्रौद्योगिकी संस्थान (बी.एच.यू.)
Indian Institute of Technology, (BHU)
वाराणसी-221005/Varanasi-221005

COPYRIGHT TRANSFER CERTIFICATE

Title of the Thesis: Petrology and tectono-metamorphic evolution of amphibolites to granulite facies rocks of the Bundelkhand craton, Jhansi, India.

Name of the Student: Pratigya Pathak

Copyright Transfer

The undersigned hereby assigns to the Indian Institute of Technology (Banaras Hindu University), Varanasi all rights under copyright that may exist in and for the above thesis submitted for the award of the **“Doctor of Philosophy”**.

Date: 8/9/2022

Place: IIT (BHU), Varanasi

Pratigya Pathak
(Pratigya Pathak)

Note: However, the author may reproduce or authorize others to reproduce material extracted verbatim from the thesis or derivative of the thesis for author's personal use provided that the source and the Institute's copyright notice are indicated.

ACKNOWLEDGEMENTS

First and foremost, I would like to express my gratitude to Professor **S. B. Dwivedi** of the Department of Civil Engineering at the Indian Institute of Technology (BHU), Varanasi, for his encouragement, assistance, guidance, and patience in correcting the numerous errors I made along the way. Countless discussions in his office and during field work have been crucial in shaping the development of this concept. Working under a guy with such devotion, enthusiasm, and passion for research, as well as such fondness for his students, has been a privilege. Without him, this work would have been impossible to finish. I will be eternally thankful to him for the information he has imparted to me since the day I joined, and I will be eternally grateful to him for the wonderful experience I had during my research term, which only increased my confidence and enthusiasm for my job.

I'd like to thank **Dr. P. B. Ramaudu** (internal subject expert) for her constant enthusiasm, support, and insightful recommendations during this project. I will always be grateful to him for the counsel he gave me and the experiences he shared with me. **Prof. Rajendra Prasad** (external subject expert), Department of Physics, Indian Institute of Technology (BHU), has also been of great assistance and support. I'm also grateful to **Dr. Medha Jha** and **Dr. B.N. Singh** for his help and advice during my PhD research. **Prof. Prabhat Kumar Singh Dikshit**, Head, Department of Civil Engineering, Indian Institute of Technology (BHU), for his encouragement and for arranging all kinds of departmental support.

I am also very thankful to **Prof. S. P. Singh** and his student **Mr. Rubal Singh**, Department of Geology, Bundelkhand University for their help throughout the field work. I represent my gratitude to **Prof. R. K. Srivastava** and **Dr. Gulab C. Gautam** Department of Geology, Banaras Hindu University (India), for facilitating the Microscopy Laboratory.

I want to thank Institute fellowship for providing financial support in the form of GATE Fellowship and other financial aids for the successful completion of the research work.

I am thankful to **Prof. Elson Paiva de Oliveira**, Department of Geology, Campinas University (Brazil) and **Prof. Cristiano Lana (University of Ouro Preto, Brazil)** who introduced me to the world of LA-ICP-MC-MS laboratory and provides the Lu-Hf dating data.

A special acknowledgement goes to my senior **Dr. Ravi Ranjan Kumar**. I am also thankful to **Mr. Dinesh Singh**, **Mr. Akhilesh Singh** and **Dr. Nikhilesh Singh**, **Dr.**

Shivanshu Shekhar, Mr. Manish Srivastava, Mr. Sandeep Maddheshiya, Mr. Raviranjana Kumar Sharma and Mr. Vikas Pandey for their continuous help, support and guidance during my lab work. It was great sharing lab with you people.

I owe a debt of gratitude to my eldest brother, **Dr. Arvind Kumar Pathak**, as he supported throughout my studies in every condition. My parents, **Mr. Ravindra Narayan Pathak** and **Mrs. Kusum Pathak**, owe me their undying love and support throughout my life. I am grateful to my sisters and my sister-in-law for providing me with the strength, advice, and freedom to pursue my aspirations. For their wishes and support, I am eternally grateful to all-powerful God for the possibilities and benefits that have come my way. There are few more uncredited good hearts behind this success. I would like to thank every one of them.

Again, I am very grateful to my supervisor and my family members, who believed and encouraged me for making this mission possible.

Pratigya Pathak

Table of Contents

Table of Contents

List of Figures	xv
List of Tables	xxiii
List of Abbreviations	xxv
List of Mineral Abbreviations	xxvii
Ab Albite.....	xxvii
Preface	xxix
INTRODUCTION	1
1.1 General.....	1
1.2 Scope of the Investigation	5
1.3 Methodology.....	7
1.4 Purpose of the Thesis.....	11
CHAPTER - 2	15
LITERATURE REVIEW	15
2.1 General.....	15
2.2 Introduction	15
2.3 Previous work done in the Bundelkhand Craton	16
2.4 Geothermobarometry and Phase equilibria modelling	18
2.5 Geochemistry	21
2.6 Why to need this study	24
CHAPTER - 3	27
GEOLOGICAL SETTING	27
3.1 Introduction	27
3.2 Geology and stratigraphy of the Bundelkhand craton	27
3.2.1. Tonalite-Trondhjemite-Granodiorite Gneisses (TTGs).....	29
3.2.2. Metasupracrustals associated with greenstone belts	30
3.2.3. Amphibolites	31
3.2.4. Pillow basalts.....	31
3.2.5. Banded iron formations (BIFs)	32
3.2.6 Madawara Ultramafic Complex (MUC).....	32
3.2.7 Intrusive Granitoids, Syenites and Pegmatites	33
3.2.8 Giant Quartz Veins (GQVs).....	34
3.2.9 Mafic Dykes	35
3.3 Geology around Mauranipur and Babina region	35
3.4 Metamorphism	37

3.5 Tectonic imprint.....	38
3.6 Geochronology.....	39
CHAPTER 4	41
PETROGRAPHY	41
4.1 Introduction	41
4.2 Petrography	41
4.3 Preparation of thin polished section.....	42
4.4 Petrography of thin sections.....	43
4.4.1 Pelitic granulites.....	43
4.4.2 Garnet-biotite gneisses	51
4.4.3 Amphibolites	54
4.4.4 Granitoids.....	64
4.4.5 Quartz Reef	72
4.4.6 Dolerite Dykes.....	72
4.4.7 Mylonitised Rocks	74
CHAPTER-5	77
MINERAL CHEMISTRY	77
5.1 Introduction	77
5.2 EPMA analytical technique	78
5.3 Garnet	79
5.3.1 Garnet zoning.....	80
5.3.2 Ca & Mn content of garnet	81
5.4 Pyroxene	82
5.4.1 Orthopyroxene.....	83
5.4.2 Clinopyroxene	83
5.5 Amphibole.....	84
5.5.1 Classification of amphibole	85
5.6 Cordierite	87
5.7 Mica.....	87
5.7.1 Biotite.....	88
5.7.1 TiO ₂ content.....	89
5.8 Feldspar.....	90
5.9 Opaque.....	91
5.10 Epidote	93
5.11 Chlorite.....	93
5.12 Sillimanite.....	94
CHAPTER - 6.....	95
GEOCHEMISTRY	95

6.1 Introduction	95
6.2 Major oxides Geochemistry	96
6.3 Trace Element Geochemistry	96
6.4 Rare Earth Elements Geochemistry	97
6.5 Analytical techniques	98
6.5.1 XRF and ICP-MS	98
6.6 Pelitic granulites	98
6.6.1 Major oxides	99
6.6.2 Trace and REEs	100
6.6.3 Discussion	101
6.7 Garnet-Biotite gneisses	105
6.7.1 Major oxides	105
6.7.2 Trace and REEs	106
6.7.3 Discussion	107
6.8 Amphibolites	108
6.8.1 Major oxides	108
6.8.2 Trace and REEs	109
6.8.3 Petrogenesis and tectonic implications	111
CHAPTER – 7	115
PART A- GEOTHERMOMETRY AND GEOBAROMETRY	115
7.A.1 Introduction	115
7.A.2 Thermodynamic Basis	115
7.A.3 Presumption	116
7.A.4 Geothermobarometers	117
7.A.5 Reaction Terminology	118
7.A.6 Geothermometry	119
7.A.7 Geobarometry	119
7.A.8 Problem/ Errors in Geothermobarometry	120
7.A.9 Concluding Remarks	123
PART B- GEOTHERMOBAROMETRY	124
7.B.1 Geothermometers	124
7.B.1.1 Garnet-biotite geothermometry	124
7.B.1.2 Garnet-orthopyroxene geothermometry	129
7.B.1.3 Garnet-cordierite geothermometry	131
7.B.1.4 Garnet-clinopyroxene geothermometry	135
7.B.1.5 Amphibole-plagioclase geothermometry:	136
7.B.2 Geobarometers	137
7.B.2.1 Garnet-biotite -plagioclase-quartz geobarometers	137

7.B.2.2 Garnet-orthopyroxene-plagioclase-quartz geobarometers	138
7.B.2.4 Amphibole-plagioclase-quartz geobarometers	143
7.B.2.5 Garnet-cordierite-sillimanite-quartz geobarometers.....	144
PART C- APPLICATION OF GEOTHERMOBAROMETERS AND AVERAGE $P-T$	147
7.C.1 Pelitic granulite	147
7.C.2 Garnet-biotite gneisses.....	148
7.C.3 Amphibolites.....	149
CHAPTER – 8	155
METAMORPHIC CONDITION	155
8.1 Introduction	155
PART-A: PHASE PETROLOGY	155
8.A.1 Introduction.....	155
8.A.2 Phase compatibility relations	156
PART B- BULK COMPOSITION MODELLING.....	160
8.B.1 Application of equilibrium thermodynamics	160
8.B.2 Pseudosection modelling.....	162
8.B.3 Methodology.....	163
8.B.4 $P-T$ Pseudosections	163
CHAPTER-9	191
TECTONO-METAMORPHIC EVOLUTION	191
9.1 Metamorphic condition	191
9.1.1 Petrographic evidences.....	192
9.1.2 $P-T-t$ Path	194
9.3 Global correlation of BuC with the Ur and Kenorland supercontinent	207
SUMMARY AND CONCLUSION.....	211
References.....	229
List of Publications	259

List of Figures

- Figure 3.1 (a) Inset map showing the location of Bundelkhand Craton in Indian shield (b) Geological map of Bundelkhand Craton with its location in India. 29
- Figure 3.2 Regional geological map of the area around Mauranipur. 36
- Figure 3.3 Regional geological map of the Babina and its adjacent area. 37
- Figure 4.1 Field photographs of the pelitic granulites from the study area. (a,b) Pelitic granulites showing discordant relationship with host rock TTG gneisses. (c) Grt-Opx pelitic granulites having granulose texture. (d) Grt-Opx pelitic granulites showing melano and leucocratic layering. (e) Field image of pelitic granulite associated with Tonalite-Tronjhemite Gneisses. (f) Megascopic field image of garnet bearing pelitic granlites. 44
- Figure 4.2. Photomicrographs (plane-polarized light, PPL) images of representative mineral assemblages and microstructures of the opx–crd–grt pelitic granulite (a) Garnet porphyroblasts in a matrix of biotite, quartz, and plagioclase. (b) Biotite consuming to form garnet. (c) Orthopyroxene that occurs in the matrix in association with garnet, biotite, and plagioclase. (d) Orthopyroxene flakes cross-cut by matrix biotite. (e) Garnet relicts rimmed by altered biotite, cordierite and plagioclase. (f) Subduded garnets in a matrix cordierite associated with biotite and quartz. 46
- Figure 4.3 Photomicrographs (plane-polarized light, PPL) and back-scattered electron (BSE) images of representative mineral assemblages and microstructures of the Grt-Opx pelitic granulites. (a) Biotite crystals showing specific orientation in a matrix of garnet, quartz and ilmenite. (b) Microfolding in sillimanite crystal in a matrix of garnet, biotite and quartz. (c) Microfolding in sillimanite crystal with broken garnet crystals. (d) Rotation of inclusion ilmenite crystals within biotite. (e) Fibrous sillimanite crystals along with patchy biotite. (f) Garnet porphyroblasts in a matrix of biotite, quartz and plagioclase. (g) Coarse-grained orthopyroxene cross-cut by garnet crystals along with matrix biotite and quartz. (h) Orthopyroxene that occurs in the matrix in association with garnet, biotite, and plagioclase. (i) Garnet relicts surrounded by orthopyroxene along with biotite and quartz. (j) & (k) BSE image of orthopyroxene and garnet crystals along with plagioclase and ilmenite. (l) Garnet porphyroblast associated with fibrous sillimanite and plagioclase. 49
- Figure 4.4 (a) Photomicrograph of retrograde metamorphism in which corroded garnet is surrounded by a rim of biotite under 51

plane polarized light. (b) Photomicrograph shows the inclusions of biotite and quartz coexisting with sillimanite within garnet (plane-polarised light). (c) Photomicrograph showing that garnet contains inclusion of biotite and quartz reacting to form garnet and k-feldspar. (d) BSE image showing garnet rimming by biotite in a matrix of plagioclase.

Figure 4.5. Field photographs of garnet-biotite gneisses of Bundelkhand craton showing (a) folding, (b) faulting and, (c) augen and tail structure. (d) Grt-Bt gneiss interlayered with TTG gneisses. (e) Grt-Bt gneiss as an enclave within the TTG gneisses. (f) Grt-Bt gneiss showing small scale folding. 52

Figure 4.6 Photomicrographs (plane-polarized light, PPL) and back-scattered electron (BSE) images of representative mineral assemblages and microstructures of the Grt-Bt gneisses. (a) Garnet porphyroblast containing inclusion of biotite along its fractures. (b) Biotite crystal completely surrounded by garnet crystals and quartz. (c) Garnet porphyroblast surrounded by biotite and quartz. (d) Garnet crystal associated with biotite and quartz in matrix (e) Garnet crystal having fractures which are transverse to the length of the crystal. (f) BSE image showing inclusion of plagioclase in garnet crystal. 53

Figure 4.7 Field photographs of the amphibolites from the study area (a) Amphibolites exposed along with TTG gneisses in Mauranipur (b) Small scale field photograph of amphibolites along with deformational features in Mauranipur (c) Felsic magma intrusion in amphibolites of Mauranipur (d) Folding in the layers of amphibolites of Mauranipur (e,f) Amphibolites of Babina (near Sukwa-dukwa dam) intruded by felsic magma. 55

Figure 4.8 Field photographs of the amphibolites from the Babina and Mauranipur regions, (a) Amphibolites exposed as enclaves within the basement rock of TTG gneisses. (b) Amphibolites also present as enclaves form but at the marginal portions it is characterized by leucocratic and melanocratic layers. (c) Here, massive mass of amphibolites occur as broken boulder and also showing intrusive signature of felsic magma. (d) At some places, small scale deformation and fractures are present in the amphibolites. 56

Figure 4.9 Photomicrographs (plane-polarized light, PPL) show representative mineral assemblages and textural relationships of the garnet-bearing amphibolites; (a) yellowish amphiboles are associated with dark green chlorites and biotites. (b) Numerous fractures and corroded boundaries, and inclusions of Amp, Bt, Chl, Ilm, Qz, and Pl mineral grains. (c) Inclusions of Amp, Bt, Chl, Ilm, Qz, and Pl in garnet, clearly shown by back-scattered electron (BSE) images. (d) Porphyroblast of amphibole is 59

associated with garnet and clinopyroxene. (e) Anhedral amphiboles present as small flakes around the garnet. (f) Enormous mass of amphiboles composed of fragmented/fractured garnet crystals.

Figure 4.10 Photomicrographs (PPL) show representative mineral assemblages and textural relationships of the garnet-absent amphibolites, (a) Porphyroblast amphiboles show an octahedral to rhombohedral shape grains. (b) Clinopyroxene is found in prismatic and lath-shaped textures, and associated with amphiboles. (c) Amphibole, clinopyroxene, and plagioclase are defining the foliation. (d) Amphiboles are present as inclusion within a massive mass of clinopyroxene. (e) Amphibole associated with the clinopyroxene porphyroblast. (f) Massive mass of amphiboles exists around clinopyroxene crystals.

62

Figure 4.11 Photomicrographs (plane-polarized light, PPL) and back-scattered electron (BSE) images of representative mineral assemblages and microstructures of the amphibolites (a & b) Amp1 and epidote present as inclusions in clinopyroxene with plagioclase, (c) Prismatic crystals of Amp2 depicting two sets of cleavage with porphyroblastic clinopyroxene, (d) Laths of plagioclase embedded within clinopyroxene crystals depicting ophitic texture, (e) Amp3 contains inclusions of clinopyroxene (f) Clinopyroxene crystals partially replaced by Amp3, (g) Epidote crystals occurring as inclusions within amphibole and plagioclase (h) Plagioclase present as inclusion within the matrix of amphibole and clinopyroxene (i) Long lath shaped grain of ilmenite at a junction of amphibole and plagioclase.

64

Figure 5.1 (a) Triangular diagram showing the variation in (spessartine + grossular)–almandine–pyrope end member compositions in the garnets from different rock types. (b) A plot of X_{Mg} vs Ca/Mn of garnets, from different rock types.

79

Figure 5.2 (a) BSE image of garnet porphyroblast, (b–f) Images of X-ray mapping of Ca, Fe, Al, Mg and Si in garnet porphyroblast; (f) X_{Alm} , X_{Py} , X_{Grs} and X_{Sps} variation along the garnet porphyroblast from rim to rim.

81

Figure 5.3 A $CaSiO_3$ - $MgSiO_3$ - $FeSiO_3$ composition diagrams of praxenites showing the plot of orthopyroxenes and clinopyroxenes from different rock types.

84

Figure 5.4 (a) Amphibole classification diagram for the amphibolites of Bundelkhand craton. (b) Plot $0.5[Al^{IV} - (Na+K)^A]$ vs $(Na+K)^A$ a.p.f.u for calcic amphibole from greenschist to granulite facies expressed as amphibolites of Bundelkhand craton belongs to amphibolites facies rock. (c) A plot of X_{Mg} vs Al^{IV} of amphibolites.

86

Figure 5.5 (a) A plot of microprobe analyses of biotites from different rock type in Mg- Ti -(Fe+Mn) diagram. (b) A plot of microprobe analyses of biotites from different rock type in Mg-(Al ^{IV} +Ti) - (Fe+Mn) diagram. (c) A plot of Ti vs Mg showing negative trend. (d) A plot of X _{Fe} /X _{Mg} vs TiO ₂ showing linear relationship.	89
Figure 5.6 Triangular NaAlSi ₃ O ₈ - KAlSi ₃ O ₈ - CaAl ₂ Si ₂ O ₈ diagram showing plots of alkali feldspar and Plagioclase feldspar.	91
Figure 5.7 Triangular diagram for ilmenite and magnetite.	92
Figure 5.8 Triangular diagram for epidotes from amphibolites.	93
Figure 5.9 Chlorite classification diagram of different rock types.	94
Figure 6.1 Chemical classification diagrams using major element composition of the studied rocks. (a) Total alkali versus silica (TAS) diagram for plutonic rocks (b) Calcic to alkali-calcic via calc-alkaline nature of pelitic granulites. (c) Granitoid classification scheme revealing magnesian to ferroan. (d) K ₂ O versus SiO ₂ plot (e) A/CNK versus A/NK diagram. (f) Na ₂ O versus K ₂ O diagram.	99
Figure 6.2 (a) Primitive mantle normalized multi-element spider diagram of pelitic granulites. (b) Chondrite normalized rare earth element plot.	100
Figure 6.3 (a) log (SiO ₂ /Al ₂ O ₃) vs log (Fe ₂ O ₃ /K ₂ O) plot (b) The MgO/CaO vs P ₂ O ₅ /TiO ₂ diagram (c) CIA versus ICV diagram (d) SiO ₂ vs. log (K ₂ O/Na ₂ O) diagram.	103
Figure 6.4 (a) Major element Discriminant Function diagram for provenance (b) TiO ₂ -Zr plot of aluminium samples (c) (Y/Nb) _N versus (Th/Nb) _N diagram (d) Zr versus Nb/Zr plot (e) Y vs Nb tectonic discrimination diagram. (f) Y+Nb vs Rb tectonic discrimination plot. Syn-COLG: syn-collisional granite; WPG: within plate granite; VAG: volcanic arc granite; ORG: ocean ridge granite.	104
Figure 6.5 Fenner's binary diagram showing moderate to strong fractionation trends for selected major elements oxide versus SiO ₂ of garnet-biotite gneisses.	106
Figure 6.6 (a) Total alkali-silica diagram (b) SiO ₂ vs K ₂ O plot, (c) Primitive mantle normalized trace element and Chondrite normalized rare earth elements plot of the Grt-Bt gneisses (e) Y vs Nb tectonic discrimination diagram and (f) Y+Nb vs Rb tectonic discrimination diagram.	107
Figure 6.7 (a) Total alkali versus silica (TAS) plot is used to	109

classify the amphibolites (b) The Zr/Ti vs Nb/Y plot.	
Figure 6.8 (a) Multi-element normalized spider diagram of garnet-bearing as well as garnet-absent amphibolites (b) Chondrite normalized rare earth element plot.	110
Figure 6.9 (a) Th/Nb vs Ba/Nb diagram showing influence of shallow subduction component in the mantle source for the amphibolites. (b) Nb/Th vs Zr/Nb diagram indicating the arc nature of the amphibolites (c) Zr vs Zr/Y diagram showing the island-arc nature of the amphibolites (d) Nb/Yb vs Th/Yb diagram depicting a subduction-related enrichment for the Amphibolites samples. (e) Ce/Nb vs Th/Nb plot showing Island-arc affinity. (f) Y vs La/Nb diagram showing back-arc affinity,	112
Figure 7.1 Coexisting Garnet-biotite pairs and derivative temperatures for different rocks.	149
Figure 7.2 Coexisting Garnet-orthopyroxene pairs and derivative temperatures for different rocks.	149
Figure 7.3 Coexisting Garnet-cordierite pairs and derivative temperatures for different rocks.	151
Figure 7.4 Coexisting Garnet-clinopyroxene pairs and derivative temperatures for different rocks.	151
Figure 7.5 Coexisting Amphibole-plagioclase pairs and derivative temperatures for different rocks.	152
Figure 7.6 Coexisting Garnet-biotite-plagioclase-quartz pairs and derivative pressure for different rocks.	152
Figure 7.7 Coexisting Garnet-cordierite-sillimanite-quartz pairs and derivative pressure for different rocks.	152
Figure 7.8 Coexisting Garnet-clinopyroxene-plagioclase-quartz pairs and derivative pressure for different rocks.	153
Figure 7.9 Coexisting Amphibole-plagioclase-quartz pairs and derivative pressure for different rocks.	153
Figure 7.10 Coexisting Garnet-orthopyroxene-plagioclase-quartz pairs and derivative pressure for different rocks.	154
Figure 8.1 AKF Diagrams, $A = (Al_2O_3 + Fe_2O_3) - (K_2O + Na_2O + CaO)$; $K = K_2O$; $F = FeO + MnO + MgO$, ($A + K + F = 100$ mol%). For the pelitic granulites solid coloured circles correspond to the observed mineral assemblages in the investigated area.	157

Figure 8.2 AKF Diagrams, $A = (Al_2O_3 + Fe_2O_3) - (K_2O + Na_2O + CaO)$; $K = K_2O$; $F = FeO + MnO + MgO$, ($A + K + F = 100$ mol%). For the garnet-biotite gneisses solid coloured circles correspond to the observed mineral assemblages in the investigated area.	158
Figure 8.3 The mineral composition of the amphibolites are shown in ACF diagram where, $A = (Al_2O_3 + Fe_2O_3) - (K_2O + Na_2O)$; $C = CaO$; $F = FeO + MgO + MnO$. ($A+C+F = 100$ mol%), (a) observed mineral assemblages in garnet bearing amphibolites, (b) observed mineral assemblages in garnet absent amphibolites.	159
Figure 8.4 (a) P-X(H ₂ O) and (b) P-X(O ₂) diagrams showing calculated pseudosection of mineral assemblages in pelitic granulite (sample M-9) at 5.4 kbar.	164
Figure 8.5 <i>P-T</i> pseudosection of mineral assemblage in pelitic granulite (sample M-9) in the NCKFMASHTO system, (b) contouring isopleths (X_{Mg}) of garnet, orthopyroxene, cordierite and biotite.	166
Figure 8.6 (a) P-X(H ₂ O) and (b) P-X(O ₂) diagrams showing calculated pseudosection of mineral assemblages in pelitic granulite (sample PM-2) at 850°C.	168
Figure 8.7 <i>P-T</i> pseudosection of mineral assemblage in pelitic granulite (sample PM-2) in the NCKFMASHTO system, (b) contouring isopleths (X_{Mg}) of garnet, orthopyroxene and biotite.	169
Figure 8.8 Pseudosection of representative sample showing different mineral assemblages at different <i>P-T</i> conditions along with isopleths of garnet, biotite and plagioclase.	171
Figure 8.9 (a) T-X _{H₂O} pseudosection at 5.0 kbar, showing the effects of varying the molar proportions of bulk-rock H ₂ O, black dash line is modelled composition of H ₂ O (3.50 %). (b) pseudosection (M1-A1) is calculated in NCKFMASHT system, and Isopleth lines for garnet (X_{Mg}), biotite (X_{Mg}), and melt modal %.	173
Figure 8.10 T-X(H ₂ O) diagrams showing calculated pseudosections of mineral assemblages in Grt-Bt gneiss (sample M-1A) at 5 kbar.	175
Figure 8.11 (a) <i>P-T</i> pseudosection of mineral assemblage in Grt-Bt gneiss (sample M-1A) in the NCKFMASHT system (b) Isopleths (X_{Mg}) of garnet and biotite contouring the <i>P-T</i> pseudosection.	176
Figure 8.12 (a) T-X(H ₂ O) pseudosection calculated at fixed	178

pressure 5.0 kbar, showing the effects of varying themolar proportions of bulk-rock H₂O in garnet-bearing amphibolites (sample B-6). The black dashed line is showing the modelled composition of H₂O (4.89 mol%). (b) T-X(O₂) pseudosection calculated at fixed pressure 5.0 kbar, showing the effects of varying the molar proportions of bulk-rock O₂ in same sample.

Figure 8.13 (a) *P-T* pseudosection for garnet-bearing amphibolites (sample B-6), showing the metastable phase, pre-peak, peak and post-peak metamorphic condition. (b) Isopleths for amphibole, biotite, garnet, clinopyroxene, and chlorite are contoured in the *P-T* pseudosection. 180

Figure 8.14 (a) T-X(H₂O) pseudosection calculated at fixed pressure 6.5 kbar, showing the effects of varying themolar proportions of bulk-rock H₂O in garnet-absent amphibolites (sample K-1). The black dashed line is showing the modelled composition of H₂O (4.50 mol%). (b) T-X(O₂) pseudosection calculated at fixed pressure 6.5 kbar, showing the effects of varying the molar proportions of bulk-rock O₂ in same sample. 182

Figure 8.15 (a) *P-T* pseudosection for garnet-absent amphibolites (sample K-1), showing the pre-peak, peak and post-peak metamorphic condition. (b) Isopleths for amphibole, plagioclase, and clinopyroxene are contoured in the *P-T* pseudosection. 183

Figure 8.16 (a) T-X_{H₂O} pseudosection at 7.5 Kbar, and (b) at 4.0 kbar, showing the effects of varying the molar proportions of bulk-rock H₂O. (c) *P-T* pseudosection showing pre-peak, peak and post-peak assemblages. (d) Isopleths X_{Ca} of Amp, X_{Mg} Cpx and X_{Fe} of Ep. 185

Figure 8.17 (a) T-X_{H₂O} pseudosection at 6.6 Kbar and (b) at 4.0 Kbar, showing the effects of varying the molar proportions of bulk-rock H₂O in amphibolite (c) *P-T* pseudosection (sample BB-1) of amphibolites showing pre-peak, peak and post-peak metamorphic assemblages in the NCFMASTHO system. (d) Isopleths X_{Mg} of amphibole, X_{Mg} of clinopyroxene and X_{Fe} of epidote contouring *P-T* pseudosection. 188

Figure 9.1 P-T-t path represents the metamorphic stages of all the three studied rocks 195

Figure 9.2 Model proposed by the Chauhan et al., 2018, illustrating the proposed geodynamic setting for the evolution of TTG and associated K-granites in the Bundelkhand craton. Stage (a): During this stage, subduction takes place with possible episodic breakoff of the slab, Stage (b): The first stage ultimately leads to closure of an ocean basin and welding of two proto-continental blocks (continental collision). Stage (c): In the late- to 200

post-collisional stage owing to thermal relaxation and extension, melting of the previously generated TTG crust ensues resulting in generation of the K-granites.

Figure 9.3 Geodynamic model of the crustal evolution of the Bundelkhand Craton proposed by the Slabnov et al., 2019, during 2.82–2.5 Ga, Maur-1-4: assemblage-1-4 of CBGC in Mauranipur belt and Bab2: formation-2 of CBGC in Babina belt. 202

Figure 9.4 Schematic, conceptual cartoon illustrating the proposed geodynamic model for evolution of the Bundelkhand Craton: (a) Geodynamic model showing the melting of subducted slab and mantle for the formation of TTGs at ~2.7 Ga, (b) followed by a shift from slab melting to direct mantle melting as a consequence of slabs break off into asthenosphere leading to mantle upwelling which caused origin of sanukitoids and also happened felsic volcanism at ~2.58 Ga, (c) finally, at ~2.5 Ga collision was happened and it provided heat flux to generate voluminous anatexic melts (anatexis processes). 204

Figure 9.5 Cartoon diagram showing the three stages of the tectono-metamorphic evolution model of the BuC. (Stage-I): it was demarcated between ~3.5 to 3.2 Ga, here subduction-related setting observed and entrapment of mafic magma in the basement of TTGs occurred. At ~3.2 Ga first metamorphism was recorded, which was experienced by amphibolites TTGs and BIFs (Stage-II): Further collision tectonism was demarcated in ~2.5 Ga, which leads to peak metamorphic condition in the BuC recorded by various rock types such as corundum-bearing schist BIFs metabasalt or amphibolites (Stage-III): It is the third stage of metamorphism, which occurs after the stabilization of the BuC, and this stage is characterized by retrograde metamorphism. Few retrograde metamorphisms reported in some metamorphic rock types such as corundum-bearing schists, monazite overgrowth in BIFs, also some mafic dykes were intruded in ~2.1 to 2.0 Ga. 206

Figure 9.6 Configuration of extended Ur. 207

Figure 9.7 A reconstruction of the Kenorland supercontinent in the Neoproterozoic (ca. 2.7 Ga) and the Bundelkhand, Dharwar and Aravalli Cratons locations. 209

List of Tables

Table 3.1 Stratigraphy with order of emplacement of different intrusives in Bundelkhand Craton	A-C
Table 3.2 Stages of metamorphism from Paleoproterozoic to Neoproterozoic reported in different rock types in the Bundelkhand Craton.	D-E
Table 3.3 Geochronological age data of all the rock types in the Bundelkhand Craton.	F-H
Table 5.1 Chemical analysis and structural formulae (on the basis of 12 Oxygen) of garnet from pelitic granulites.	I-L
Table 5.2 Chemical analysis and structural formulae (on the basis of 6 Oxygen) of Orthopyroxene from pelitic granulites.	M-N
Table 5.3 Chemical analysis and structural formulae (on the basis of 6 Oxygen) of Clinopyroxene from amphibolites.	O-P
Table 5.4 Chemical analysis and structural formulae (on the basis of 23 Oxygen) of amphibole from amphibolites.	Q-R
Table 5.5 Chemical analysis and structural formulae (on the basis of 18 Oxygen) of Cordierite from pelitic granulites.	S
Table 5.6 Chemical analysis and structural formulae (on the basis of 22 Oxygen) of biotite from pelitic granulites.	T-V
Table 5.7 Chemical analysis and structural formulae (on the basis of 8 Oxygen) of Plagioclase from pelitic granulites.	W-Y
Table 5.8 Chemical analysis and structural formulae (on the basis of 4 Oxygen) of Ilmenite from pelitic granulite and amphibolites.	Z
Table 5.9 Chemical analysis and structural formulae (on the basis of 25 Oxygen) of Epidote from amphibolites.	AA
Table 5.10 Chemical analysis and structural formulae (on the basis of 28 Oxygen) of Chlorite from amphibolites.	BB-CC
Table 5.11 Chemical analysis and structural formulae (on the basis of 10 Oxygen) of Sillimanite from pelitic granulites.	DD
Table 6.1 Representative major oxides (in wt%), trace elements and REEs (in ppm) compositions of pelitic granulites.	EE
Table 6.2 Representative major oxides (in wt%), trace elements and REEs (in ppm) compositions of pelitic granulites (continued....).	FF

Table 6.3 Representative major oxides (in wt%), trace elements and REEs (in ppm) compositions of garnet-biotite gneisses.	GG
Table 6.4 Representative major oxides (in wt%), trace elements and REEs (in ppm) compositions of garnet bearing and garnet absent amphibolites.	HH
Table 7.1 Pressure and temperature estimates of the Grt-Opx pelitic granulites (PM2) and Grt-Bt-Sill (K-2) through conventional geothermobarometers.	II
Table 7.2 The conventional geothermobarometry estimates of Grt-Opx-Crd pelitic granulites (M-9) from the Mauraniour region.	JJ
Table 7.3 The conventional geothermobarometry estimates of Grt-Bt gneisses (M-1A) from the Mauraniour region.	KK
Table 7.4 The conventional geothermobarometry estimates of Garnet-bearing amphibolites (B-6) and Garnet-absent amphibolites.	LL

List of Abbreviations

- AX** Activity-Composition
- BSE** Back scattered image
- BuC** Bundelkhand craton
- BTZ** Bundelkhand Tectonic Zone
- CBGB** Central Bundelkhand Greenstone Belt
- CIS** Central Indian Shear Zone
- CITZ** Central India Tectonic zone
- E-MORB** Enriched mid-ocean ridge basalt
- EPMA** Electron microprobe analysis
- GPS** Global Positioning System
- GBF** Great Boundary Fault
- HFSE** High field strength element
- HREE** Heavy rare earth elements
- IBC** Isobaric Cooling
- ICP-MS** Inductively Coupled Plasma-Mass Spectrometry
- ITD** Isothermal Decompression
- LA-ICP-MS-MC** Laser ablation multi-collector inductively coupled plasma
- LILE** Large-ion lithophile element
- LREE** Light rare earth element
- MMB** Mahakoshal Mobile Belt (MMB)
- N-MORB** Normal mid-ocean ridge basalt,
- OIB** Ocean island basalt.
- P-T** Pressure and temperature
- P-T-t** Pressure-Temperature-Time
- REE** Rare earth element
- SMB** Southern Sausar Mobile Belt
- SBGB** Southern Bundelkhand Greenstone Belt

SEM Scanning electron microscope

SNNF Son Narmada North Fault

UHT Ultra high-temperature

XRF X-ray fluorescence

List of Mineral Abbreviations

Ab	Albite
Alm	Almandine
Amp	Amphibole
Ann	Annite
An	Anorthite
Ap	Apatite
Aug	Augite
Bt	Biotite
Chl	Chlorite
Cpx	Clinopyroxene
Crd	Cordierite
Di	Diopside
Grs	Grossular
Grt	Garnet
Gr	Graphite
Hbl	Hornblende
Ilm	Ilmenite
Kfs	K-feldspar
Ky	Kyanite
Liq	Liquid
Mag	Magnetite
Mc	Microcline
Mnz	Monazite
Opx	Orthopyroxene
Plg	Plagioclase
Prp	Pyrope
Qz	Quartz
Sill	Sillimanite
Sps	Spessartine
Ts	Tschermakite
Zrn	Zircon

Preface

The Indian subcontinent is divided into two Archean cratonic blocks by the Central Indian Tectonic Zone (CITZ), which runs in the ENE–WSW direction; the northern and southern cratonic blocks. The southern Indian block includes Bastar, Dharwar, and Singhbhum cratons, while the northern Indian block includes the cratons of Bundelkhand and Aravalli. The Great Boundary Fault is the main boundary that divides the northern Indian block into two blocks. The eastern block is known as the Aravalli cratonic block, and the western block is known as the Bundelkhand cratonic block.

The Bundelkhand Craton (BuC) is of semi-circular shape, having an area of about 45,000 km² of which only 26,000 km² is exposed as an outcrop between 24°11' to 26°27'N and 78°10' to 81°24'E and the rest is covered by alluvium of the Ganga basin. In the west, the BuC is fringed by the Great Boundary Fault (GBF), trending NE–SW, in the north-west by the Gwalior Basin, in the south by the Sonarai Basin, and by the Bijawar marginal basins in the south-east. The Vindhyan Supergroup overlies the marginal basins and surrounds the BuC on three sides. The Gangetic alluvial plains cover the craton on the northern side but the southwestern part is hidden beneath the Deccan basalts. The BuC is divided into two large E–W trending greenstone belts, the northern belt and the southern belt, which contain supracrustal units tectonically embedded with TTGs. The northern belt, also known as the Central Bundelkhand Greenstone belt (CBGB), runs through Mauranipur, Kuraicha, and is exposed in the middle of BuC. Metamorphosed basic rocks, felsic volcanic rocks, metasedimentary rocks (BIFs), pink granites and granodiorites are exposed here. The southern belt stretches from Madaura to Girar and contains a sequence of ultramafic-mafic volcanic rocks, quartzite, BIF, chlorite schist, and marble.

The study area around Mauranipur and Babina lies within the Central Bundelkhand Greenstone Belt. The investigated area falls between latitude 25°09'45" N to 25°15' N, and longitude 78°25' S to 78°35' S in Babina, as well as latitude 25°11'54" N to 25°14'48" N, and longitude 79°05' S to 79°09'35" S in Mauranipur of the BuC. The study area mainly covers the village of Kuraicha, the Saprar river section, and the Sukwa Dam area. The study area consist of TTGs, banded magnetite quartzite (BMQ), quartz reefs ultramafic rocks, amphibolites, granitoids, pelitic granulites, garnet-biotite gneiss, garnetiferous amphibolite, quartzite, granitic gneiss, and migmatite.

Microscopic investigations of the studied rock samples have revealed distinct types of mineral assemblages in three rock types such as: Garnet-orthopyroxene-cordierite-biotite-sillimanite-plagioclase-ilmenite-quartz, Garnet-orthopyroxene-biotite-sillimanite-plagioclase-ilmenite-quartz, Garnet-biotite-sillimanite-plagioclase-ilmenite-quartz, Garnet-cordierite-biotite-sillimanite-plagioclase-ilmenite-quartz, in pelitic granulites; garnet-biotite-plagioclase-quartz-k-feldspar in garnet-biotite gneisses and garnet-amphibole-plagioclase-biotite-quartz-ilmenite, clinopyroxene-amphibole-plagioclase-epidote-rutile-ilmenite-quartz in amphibolites.

Electron microprobe analyses (EPMA) of minerals from the different mineral assemblages are used to observe the characteristics of mineral phases. The pyrope content of garnet from the different rock types indicates the following trend: pelitic granulites > garnet-biotite gneisses > amphibolites. The X_{Mg} values range between 0.40 and 0.47 and correspond to hypersthene in pelitic granulites. The X_{Mg} value of cordierite varies between 0.61 and 0.69 in pelitic granulites. The X_{Mg} in biotites shows the following trend: pelitic granulites (0.38 to 0.61) > amphibolites (0.45 to 0.49) > garnet-biotite gneisses (0.31 to 0.44) >. The clinopyroxenes of amphibolites are plotted in the diopside field. The X_{Mg} value of clinopyroxene ranges from 0.59 to 0.65. The amphiboles from amphibolites seize a place in

the Tschermakite domain. They have X_{Mg} values from 0.69-0.89. The amphibole contains (p.f.u) Na = 0.276–0.497, K = 0.022–0.062, and Ti = 0.031–0.054.

Geochemical analysis of pelitic granulites reveals much about the protoliths and their geodynamic settings. The total alkali-silica diagrams of pelitic granulites show diorite, granodiorite, and quartz–monzonite fields, showing that the protolith of pelitic granulites came from a variety of sedimentary provenances. In the primitive-mantle-normalized trace-element spider diagram, positive anomalies are detected for Ba, K, Pb, Nd, Sm, Gd, and Y, but significant negative anomalies are detected for high field strength elements (HFSEs) such as Nb, Ta, and Ti, indicating a characteristic feature of subduction orogeny. A decrease in Nb and Ti concentrations confirmed an island arc setting. All samples have positive Eu anomalies in the chondrite-normalized REE patterns. The pelitic granulites acquire the domain of felsic igneous provenance when plotted in the discrimination function diagram. The TiO_2 versus Zr plot confirms this as all the pelitic granulite samples are again plotted in the felsic igneous rocks field. The Zr against Nb/Zr curve suggests that the protolith of pelitic granulites was exposed to a subduction-related tectonic setting. The Y vs Nb plot suggests that the pelitic granulite protolith came from volcanic arc granite (VAG) and a syn-collisional tectonic environment. The TAS diagram for Grt-Bt gneisses displays a contracting protolithic nature varying from diorite, granodiorite, and granite. The primitive mantle normalized spider diagram of Grt-Bt gneisses reveals depletion of Mo, Ho, Tm, Ba, K, Nb, Sr, Hf, Ti, and an abundance of Rb, Th, U, La, Ce, Nd, and Gd. The REE chondrite normalized patterns show enriched LREE and depletion in HREE with high to moderate $(La/Yb)_N$. The negative anomaly of Nb and Ti indicates that a subduction tectonic setting has occurred in the BuC. The Grt-Bt gneisses have high SiO_2 and low Cr and Ni concentrations, interpreted as protoliths derived from the hydrous thickened lower crust or may be due to crustal contamination with ascending partial melt. The Y vs Nb and $(Y+Nb)$ vs Rb tectonic

discrimination diagrams show that the protolith of most Grt-Bt gneisses had an affinity towards the volcanic arc granite (VAG), whereas the M-1C sample shows within plate granite (WPG) affinity. Total alkali versus silica (TAS) plot used to classify the amphibolites reveals that all of the garnet-bearing amphibolites are plotted in the basalt region; three garnet-absent amphibolites are projected into the basaltic field, and three are projected into the basaltic andesitic field. The Zr/Ti vs Nb/Y diagram reveals that all garnet-bearing amphibolites plot in the basaltic andesite field, and garnet-absent amphibolites plot in the sub-alkaline basalt field. A decrease in Nb and Ti concentrations has validated an island arc setting. Light rare earth element (LREE) enrichment is higher in garnet-bearing amphibolites than heavy rare earth element (HREE) enrichment ($La_N/Lu_N = 2.85-7.21$), with a little negative Eu anomaly ($Eu_N/Eu_{N^*} = 0.76-0.86$). However, garnet-absent amphibolites have a slight enrichment of LREE relative to HREE ($La_N/Lu_N = 1.20-2.13$) with a slight positive Eu anomaly ($Eu_N/Eu_{N^*} = 1.00-1.13$). The sub-parallel REE patterns show that a phase of compositional variation dominated crystal fractionation. The studied amphibolites have moderately enriched LREE and LILEs (Ba, Rb, Th, U, and K) but negative Nb, Ta, Zr, and Ti anomalies. Garnet-bearing amphibolites show 4.45–5.04 ppm, and garnet-absent amphibolites have low Th (0.65–1.25 ppm), indicating little crustal contamination or no Th addition in amphibolites. The Th/Nb vs Ba/Nb discrimination diagram shows a clear influence of the shallow subduction component on garnet-bearing and garnet-absence amphibolites, but no sign of deeper subduction component influence. The Nb/Th vs Zr/Nb tectonic discrimination diagram suggests an arc-like setting for the amphibolites from the Babina and Mauranipur regions; whereas the Zr vs Zr/Y plot suggests an island arc setting.

The various conventional geothermobarometry pairs have been used for evaluating the temperature and pressure conditions for pelitic granulites. the Grt-Bt thermometry provides prograde temperatures of 640°C–692°C for garnet core and biotite included in garnet

and 605°C–660°C for garnet and matrix biotite, whereas pressure of 5.79 kbar at 650°C using the garnet-biotite-plagioclase-quartz geobarometer (GBPQ). Similarly, Grt-Opx thermometry provides peak temperatures of 762°C–845°C for core values and 712°C–825°C for rim values of garnet and orthopyroxene and peak pressure has been observed as 6.49–7.49kbar at 800°C using the garnet–orthopyroxene–plagioclase-quartz (GOPQ) barometer. However, the garnet-cordierite geothermometer provides the retrograde temperature of 508°C–604°C for garnet core and cordierite included in garnet and 489°C–588°C for garnet and matrix cordierite, whereas garnet-cordierite-sillimanite-quartz geobarometer was used to estimate the pressure and it ranges from 4.24 to 4.89kbar. For the Grt-Bt gneiss, the garnet–biotite exchange geothermometer was applied to inclusion and matrix biotite. It provides 595°C–656°C from biotite present as inclusion in garnet and 578°C–618°C from matrix biotite and pressure of 5.0 kbar at 600°C using the garnet-biotite-plagioclase-quartz geobarometer (GBPQ). In the garnet-bearing amphibolites, the garnet-biotite pair was used to define a temperature of the pre-peak stage from garnet and biotite rim compositions, where biotite exists as inclusion within the garnet; it shows 539 to 597°C at 5.5 kbar. The Grt–Cpx geothermometer can measure the temperature of the peak metamorphic stage as 834°C and 760°C at 7.0 kbar pressure. Simultaneously, GCPQ (Grt-Cpx-Pl-Qz) geobarometry calculated 7.42 and 6.46 kbar pressures at a constant temperature of 800°C. The post-peak temperature condition is 556°C at 4.5 kbar pressure, as measured by an Amp-Pl geobarometer. The pressure condition for post-peak metamorphism is estimated to be 5.04 kbar at 550°C using an Amp-Pl-Qz geobarometer model. *P–T* conditions in garnet-absent amphibolites are 517°C and 685°C from the rim and core compositions, respectively, and model of the Amp-Pl-Qz geobarometer predicts 5.21 and 6.78 kbar pressure from the rim and core portions.

Pseudosection modeling of the pelitic granulites in the NCKFMASHTO system with the help of Perple_X ver.6.9.0 software shows that the *P–T* condition of pre-peak

metamorphism is found in the range of 4.00–5.12 kbar and 560–600°C. The peak assemblage has a P – T stability field ranging from 6.40–6.62 kbar and 700–730°C. The retrograde metamorphic assemblage is stable in the range of 4.20–4.40 kbar pressure and 670–692°C temperature. The P – T pseudosection for the garnet-biotite gneisses represented a peak metamorphic assemblage and occupied a field in the P – T range of 6.35–6.75 kbar and 755–780°C. Similar mineral assemblage has been observed under lower pressure and temperature conditions. The melt phase does not exist here, whereas H₂O is available as a component. Their P – T condition is comparatively low, between 4.80–5.28 kbar and 718–735°C. The assumed value of H₂O and O₂ has been defined by the constructed T-X(H₂O) and T-X(O₂) pseudosection at a fixed pressure of 5.0 kbar for sample B-6. The value of H₂O was determined based on the variation of H₂O in the bulk rock composition ranging from 0.0 to 6.0 mol%, whereas O₂ was calculated based on the variation of O₂ in the bulk rock composition ranging from 0.0 to 1.0 mol%. The meta-stable, pre-peak, and post-peak mineral assemblages are depicted in the T-X(H₂O) diagram with the appropriate amount of X(H₂O) = 4.89 mol%. Similarly, the T-X(O₂) diagram reveals that a 0.50 mol% amount is appropriate, denoted by a large black dashed line. Therefore, 4.89 mol% of H₂O and 0.50 mol% of O₂ are reliable amounts for further P – T pseudosection calculation. The P – T pseudosection for garnet-bearing amphibolites in the NCKFMASHTO system shows a meta-stable mineral assemblage that may have formed before pre-peak metamorphism and is dominated by chlorite. This acquired phase is stable in the P – T range 3.2–6.2 kbar/420–550°C, and amphibole and chlorite isopleths further narrow the P – T range to 4.35–4.1 kbar/515–475°C. The pre-peak metamorphic assemblages are defined as Grt-Amp-Chl-Bt-Pl-Qz-Ilm-H₂O and are stable in the P – T conditions of 6.2–7.5 kbar and 570–595°C. The P – T conditions for garnet-bearing amphibolite's peak metamorphic stage are 7.4–6.8 kbar/805–760°C. The post-peak metamorphic assemblage is stable at a P – T range of 6.15–4.0 kbar and 750–580°C. The

P - T pseudosection plotted for the garnet-absent amphibolites in the NCFMASHTO system shows that the pre-peak metamorphism occurs in the P - T range of 4.0–6.4 kbar/400–450°C. Peak metamorphic assemblage is stable at 7.4–7.0 kbar/810–785°C. The post-peak assemblage is denoted as Amp-Pl-Qz-Ilm-H₂O, and amphibole and plagioclase isopleths are used to define the P - T conditions of 4.0–3.1 kbar/710–620°C.

The clockwise P - T - t path has been obtained from orthopyroxene-bearing pelitic granulites by thermodynamic calculation and pseudosection modelling. The pre-peak metamorphic stage was recorded between 4.00–5.12 kbar and 560–600°C. This rock undergoes further burial depth, and with a significant change in temperature conditions, this situation indicates an increase in pressure; hence it demarcated the peak metamorphic stage. The P - T conditions of this stage reached a high-pressure condition with a range of 6.40–6.62 kbar and 700–730°C, following a nearly isothermal decompression (ISD) path to achieve the post-peak stage. The post-peak stage was documented by the appearance of Crd, and Grt, and P - T conditions were reached at 4.20–4.40 kbar and 670–692°C. The geodynamic significance of the peak (high-pressure) metamorphism from the Mauraipur region of the CBGB suggests subduction and exhumation in a single cycle as a complete clockwise P - T - t path. The garnet-biotite gneisses are characterized by the mineral assemblage garnet + biotite + plagioclase + k-feldspar + ilmenite + quartz + melt. P - T pseudosection modelling shows mineral assemblage Grt-Bt-Pl-Kfs-melt-Ilm-Qz to be stable at the P - T range of 6.35–6.75 kbar and 755–780°C. The clockwise P - T path is constrained by the P - T pseudosection of garnet-bearing amphibolite. This P - T path generates three prominent metamorphic assemblages, as well as a previously developed meta-stable mineral assemblage. The meta-stable mineral assemblage Amp-Chl-Bt-Pl-Qz-Ilm appears at the 4.35–4.1 kbar/515–475°C P - T condition, suggesting a primitive mineral assemblage. Garnet was not visible at this temperature, but as it rises, it formed a unique mineral assemblage Grt-Amp-Chl-Bt-Pl-Qz-Ilm, which is stable in a narrow region with a P - T range

of 6.5–6.25 kbar/590–580°C. This assemblage forms under amphibolite facies conditions during the pre-peak metamorphic stage. Later, the Babina region experienced the burial tectonism, which was characterized by a continuous increase in pressure and temperature, and the amphibolites underwent peak metamorphism until the granulite facies metamorphism, characterized by the mineral paragenesis Grt-Amp-Cpx-Bt-Pl-Qz-Ilm-H₂O, and this field is stable at 7.4–6.8 kbar/805–760°C. The mineral assemblage of the post-peak metamorphic stage Amp-Bt-Pl-Qz-Ilm, is stable at a P – T range of 4.75–4.45 kbar/615–585°C, which acquires a Cpx and Grt free field. This post-peak stage occurred after the peak stage as a result of a decompression process that resulted in a decrease in pressure conditions, also known as isothermal cooling, implying that this stage may have developed as a result of decompression and subsequent exhumation of amphibolites on the surface.

The present study proposes a geodynamic model of the BuC based on the P – T conditions, geochemical analysis and geochronology of the pelitic granulites, garnet-biotite gneisses and amphibolites from the BuC. Both amphibolites register a clockwise path with peak metamorphism, followed by prograde and then retrograde metamorphism, showing three distinct compositions in the three stages of amphiboles. The protoliths of both amphibolites from the Mauranipur and Babina regions were formed by subduction-related tectonic settings and further affected by various thermal and collisional events. The studied amphibolites exist as enclaves and intrusive bodies and have undergone various metamorphic events, which are schematically represented as a plausible geodynamic model for three different stages. Ur is the oldest known Archean supercontinent, having formed 3.0 Ga ago by joining the Indian subcontinent's Dharwar and Singbhum cratons, South Africa's Kaapvaal craton, and Western Australia's Pilbara. Based on the age data and geodynamic settings of the Archean rocks reported from these cratons, it seems that the Bundelkhand, the Aravalli, and the Western and Eastern Dharwar Cratons appear to have been portions of the Kenorland Supercontinent in Archean times. In the Meso-Neoproterozoic period (2.9–2.7 Ga), subduction-

accretion processes gave birth to the active expansion of the continental crust in the northern portion of the Kenorland supercontinent, whilst plume processes and subduction processes prevailed in the southern section. This evidence supported that the Mesoarchean subduction-accretion processes in the BuC were similar to those of the Karelian Craton and the Superior Province in the northern half of the Kenorland supercontinent. In the Neoarchean (ca. 2.6 Ga), the core of the supercontinent was formed, and until then, the crust of the southern part of the supercontinent continued to grow during subduction and accretion processes in the Bundelkhand, Aravalli and Western and Eastern Dharwar Cratons.

